



# Electrical control of glass-like dynamics in vanadium dioxide for data storage and processing

Mohammad Samizadeh Nikoo<sup>1</sup>✉, Reza Soleimanzadeh<sup>1</sup>, Anna Krammer<sup>2</sup>, Guilherme Migliato Marega<sup>3</sup>, Yunkyu Park<sup>4</sup>, Junwoo Son<sup>4</sup>, Andreas Schueler<sup>2</sup>, Andras Kis<sup>3</sup>, Philip J. W. Moll<sup>5,6</sup> and Elison Matioli<sup>1</sup>✉

**Metal-oxide-semiconductor junctions are the building blocks of modern electronics and can provide a variety of functionalities, from memory to computing. The technology, however, faces constraints in terms of further miniaturization and compatibility with post-von Neumann computing architectures. Manipulation of structural—rather than electronic—states could provide a path to ultrascaled low-power functional devices, but the electrical control of such states is challenging. Here we report electronically accessible long-lived structural states in vanadium dioxide that can provide a scheme for data storage and processing. The states can be arbitrarily manipulated on short timescales and tracked beyond 10,000 s after excitation, exhibiting features similar to glasses. In two-terminal devices with channel lengths down to 50 nm, sub-nanosecond electrical excitation can occur with an energy consumption as small as 100 fJ. These glass-like functional devices could outperform conventional metal-oxide-semiconductor electronics in terms of speed, energy consumption and miniaturization, as well as provide a route to neuromorphic computation and multilevel memories.**

Strongly correlated materials—in which several physical interactions involving spin, charge, lattice and orbit are simultaneously active—can exhibit notable electrical properties<sup>1</sup>. Among them, the first-order insulator–metal transition (IMT) in vanadium dioxide ( $\text{VO}_2$ ), which happens close to room temperature, is of particular interest<sup>2–6</sup>. From a physical point of view, understanding the underlying mechanism of phase switching in  $\text{VO}_2$  is still a challenge, as several models ranging from Peierls to Mott–Hubbard types were not successful in explaining the broad range of phenomena occurring in the material<sup>7</sup>. Different types of excitation—including temperature, electric field and doping—can induce an IMT, which makes the understanding of phase switching more difficult<sup>2,8</sup>. From a technological point of view, the bulk conductivity and abrupt phase transition in  $\text{VO}_2$  can potentially overcome some of the fundamental limitations in conventional metal-oxide-semiconductor electronics, including the limited conductance imposed by Thomas–Fermi screening<sup>9</sup> and the thermionic subthreshold-slope limit imposed by Boltzmann tyranny<sup>10</sup>.

In addition to the application of such phase-change materials in traditional electronics, the rich variety of phenomena in  $\text{VO}_2$  (refs. <sup>11–15</sup>) can provide novel functionalities for future electronic devices. In this Article, we report electrically controllable glass-like states in  $\text{VO}_2$ , which could be used to create a platform for information processing and storage. We show that two-terminal devices exhibit a continuous spectrum of states that are revealed by the incubation time of the IMT: the time at which the nucleation of phase transition percolates to form the first conductive filament between the two terminals of the switch. The state can be imposed by a sequence

of binary switching events and can be tracked for hours after excitation.

## Electrical manipulation and probing of $\text{VO}_2$ devices

Figure 1a shows an ultrafast time-domain experimental setup that can precisely collect the temporal response of a two-terminal  $\text{VO}_2$  switch (inset). The device was integrated with radio-frequency pads (ground–signal–ground configuration) that—together with high-frequency probes—enable accurate measurements with time resolutions down to ~5 ps (ref. <sup>16</sup>). A square-pulse generator applies repetitive 10-μs-long pulses with a fixed amplitude (set voltage  $V_{\text{set}} = 2.1$  V) to a two-port 3-μm-long  $\text{VO}_2$  switch. The waveform of the current passing through the device is measured at the 50 Ω port of a high-frequency oscilloscope, and the transient conductance of the device is extracted. Following an applied pulse, the  $\text{VO}_2$  film initially exhibits an insulating behaviour; only after an incubation time  $t_{\text{inc}}$ , it undergoes an IMT (Fig. 1b). The measurements indicate that the incubation time strongly depends on the history of the previous phase transitions. The very first switching curve (Fig. 1b) shows an incubation time of ~1.4 μs. Triggering an IMT and measuring the incubation time after a 10-ms-long relaxation time ( $T$ ) results in a ten times shorter incubation time. Longer relaxation times after the first phase transition cause longer incubation times; however, the value of  $t_{\text{inc}}$  is still lower than that of the very first switching, even after  $T = 10,000$  s.

Incubation time versus relaxation time (Fig. 1c) indicates a logarithmic relation  $t_{\text{inc}} = (78 \text{ ns}) \log[T/(160 \mu\text{s})]$ . Although  $t_{\text{inc}}$  has strong dependence on the previous switching events, device conductance

<sup>1</sup>Power and Wide-band-gap Electronics Research Laboratory (POWERlab), Institute of Electrical and Micro Engineering, École Polytechnique Fédérale de Lausanne (EPFL), Lausanne, Switzerland. <sup>2</sup>Solar Energy and Building Physics Laboratory, Institute of Civil Engineering, École Polytechnique Fédérale de Lausanne (EPFL), Lausanne, Switzerland. <sup>3</sup>Laboratory of Nanoscale Electronics and Structures (LANES), Institute of Electrical and Micro Engineering and Institute of Materials Science and Engineering, École Polytechnique Fédérale de Lausanne (EPFL), Lausanne, Switzerland. <sup>4</sup>Department of Materials Science and Engineering (MSE), Pohang University of Science and Technology (POSTECH), Pohang, Republic of Korea. <sup>5</sup>Laboratory of Quantum Materials (QMAT), Institute of Materials (IMX), École Polytechnique Fédérale de Lausanne (EPFL), Lausanne, Switzerland. <sup>6</sup>Max Planck Institute for the Structure and Dynamics of Matter, Hamburg, Germany. ✉e-mail: [mohammad.samizadeh@epfl.ch](mailto:mohammad.samizadeh@epfl.ch); [elison.matioli@epfl.ch](mailto:elison.matioli@epfl.ch)

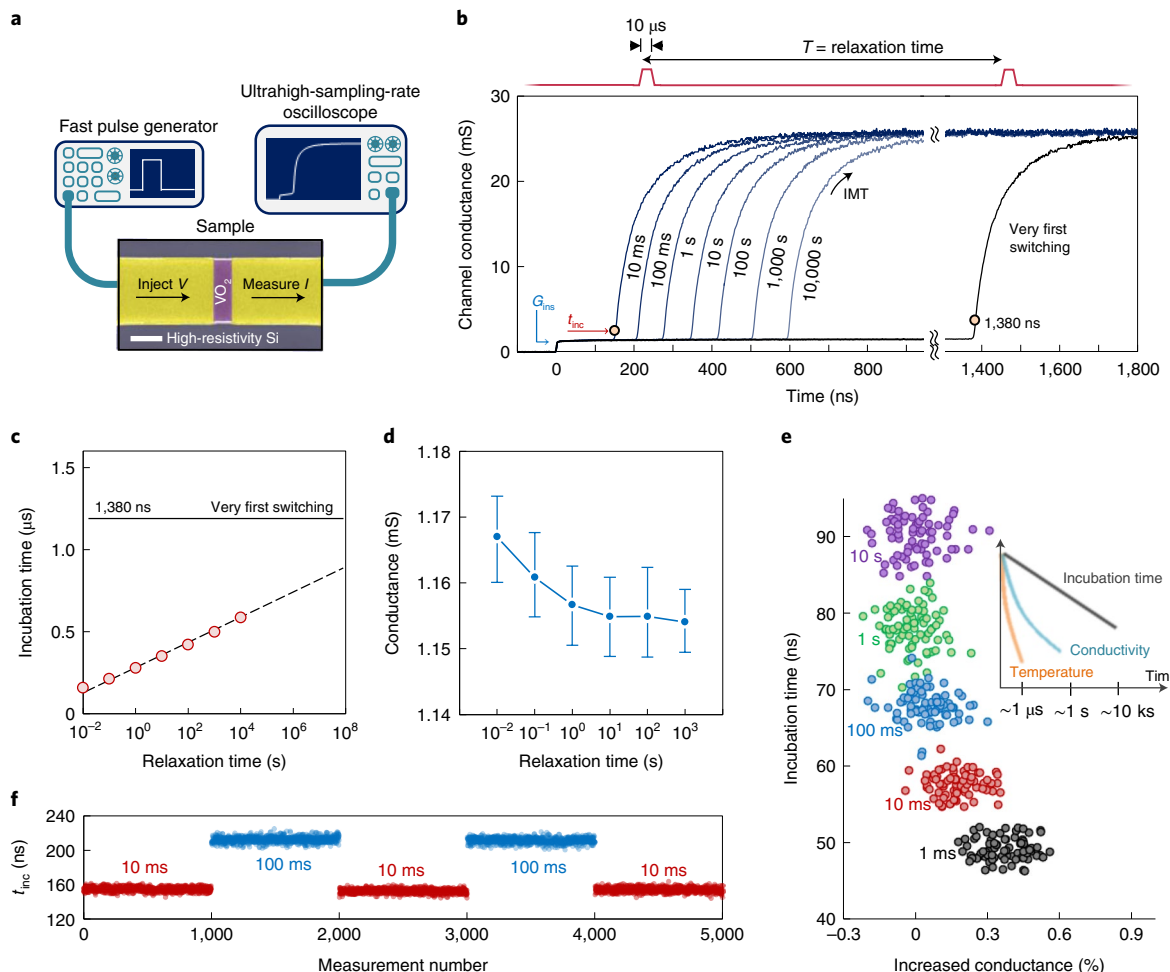


**Fig. 1 | Tracing the state dynamics of  $\text{VO}_2$  switches with incubation time.** **a**, Schematic of the ultrafast time-domain experimental setup. The SEM image shows the  $\text{VO}_2$  switch. Scale bar, 5  $\mu\text{m}$ . The devices investigated had lengths varying from 50 nm to 3  $\mu\text{m}$ . **b**, Transient conductance of the  $\text{VO}_2$  channel corresponding to different relaxation times  $T$ , as well as the very first switching cycle. The incubation time ( $t_{\text{inc}}$ ) and conductance of the insulating state ( $G_{\text{ins}}$ ) were studied. **c**, Incubation time versus relaxation time. Here  $t_{\text{inc}}$  is a logarithmic function of  $T$ . The error bars are smaller than the symbol dimension. **d**,  $G_{\text{ins}}$  versus relaxation time. After ~1 s, variations in conductance are no longer detectable. **e**, Incubation time versus increased conductance ( $(G_{\text{ins}} - \bar{G})/G_{\text{ins}}$ , where  $\bar{G}$  is the average over  $G_{\text{ins}}$  for measurements corresponding to 10 s relaxation) for different relaxation times for a 100-nm-long device, showing the reproducibility of the results in nano-devices. The inset illustrates the fast relaxation of temperature and resistance, as well as the slow dynamics of  $t_{\text{inc}}$ . **f**, Monitored incubation time for 5,000 measurements with two different relaxation times (10 and 100 ms), showing that the effect is reversible and consistent.

$G_{\text{ins}}$  in the insulating state (averaged over  $20 < t < 120$  ns) shows very small variations that become undetectable after ~1 s (Fig. 1d). The observed effect is qualitatively identical in micrometre- and nanometre-long devices. Figure 1e shows the incubation time versus relative increase in conductivity for a 100-nm-long channel device. The values of incubation times are well distinguishable, whereas conductivity shows a very small variation, which completely relaxes after 1 s.

We note that the thermal relaxation of the device is fairly fast (~100 ns; Extended Data Fig. 1), and therefore, heat accumulation does not play any role in these observations (Fig. 1e, inset). The memory effect observed in  $t_{\text{inc}}$  is reversible and is not due to any degradation in the film (Fig. 1f). The results presented here correspond to a 100-nm-thick  $\text{VO}_2$  film synthesized by sputtering on a high-resistivity silicon substrate. The results were reproduced in devices with different metal contacts with high device-to-device consistency (Extended Data Fig. 2), as well as in pulsed laser deposition (PLD)-grown films on other substrates (Extended Data Fig. 3), supporting the generality of the effect.

In the following experiment, the devices were excited with a packet of  $N$  identical pulses ( $V_{\text{set}} = 2.1$  V), and  $t_{\text{inc}}$  was monitored after a relaxation time of  $T = 1$  s (Fig. 2a). The total duration of excitation including  $N$  pulses ( $\Delta T = 1$  ms) was much shorter than the relaxation time  $T$ . Different pulse packets resulted in different values of  $t_{\text{inc}}$ , indicating that such multipulse excitation can be used to manipulate the state of the device. Figure 2b shows the summary of the observed results in which the measured values of  $t_{\text{inc}}$  for different values of  $N$  are presented for 60 consecutive acquisitions. These results indicate a fully electrical scheme to manipulate and sense a Mott system (Fig. 2c). It is worth noting that the excited state does not depend on  $\Delta T$ ; therefore, the state can be induced in very short timescales (Extended Data Fig. 4). Incubation time in the evaluated devices also did not show any dependence on the width of the excitation pulses, and state manipulation was achieved only through the number of triggering events.

### Exploration of possible mechanisms

We explored the possible mechanisms of the observed effect. The first question was whether the electric current in the film

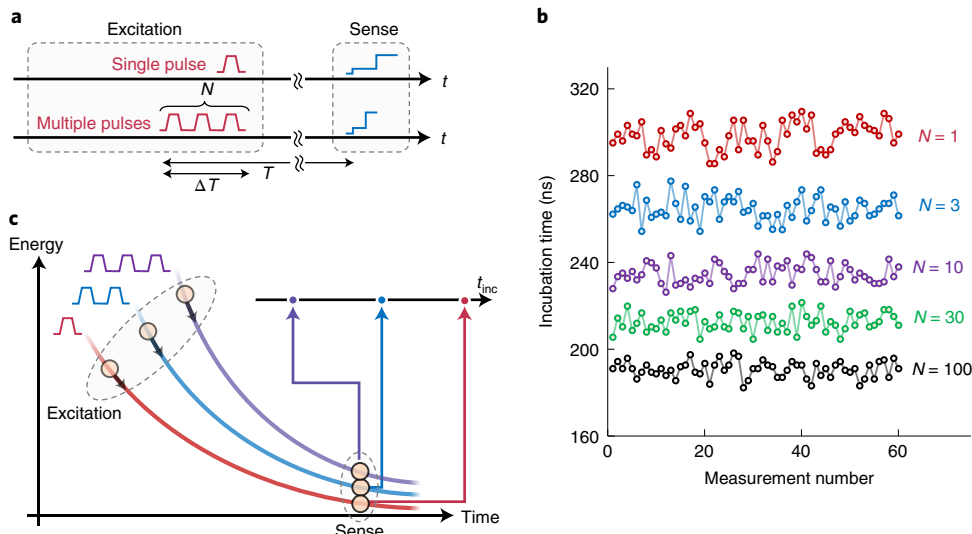


**Fig. 2 | Manipulation of post-firing state of VO<sub>2</sub> switches.** **a**, Schematic showing the excitation of the VO<sub>2</sub> switch with single or multiple pulses and monitoring  $t_{\text{inc}}$  at the sensing pulse after a long relaxation time  $T$ . **b**, Measured  $t_{\text{inc}}$  for different excitation pulse numbers ( $N$ ) for  $\Delta T=1\text{ ms}$  and  $T=1\text{ s}$ . **c**, After multiple pulses, the film undergoes different relaxation trajectories, and monitoring  $t_{\text{inc}}$  can identify the different original excitations.

induced the observed memory. This is a critical aspect because quasi-non-volatile memories induced by long high-current biases have been observed<sup>17</sup>. However, this is not the case in our devices, as the memory effect is independent of the excitation type and can also be purely induced by heat. Figure 3a shows the synchronized measurements in which IMT is achieved by a pulsed heater that is electrically isolated from the VO<sub>2</sub> switch. Every 2 s, a 20-μs-long pulse triggers the IMT in the electrically isolated heaters, which ensures a temperature-driven IMT in the VO<sub>2</sub> switch at the middle of the two heaters (Extended Data Fig. 5). We electrically triggered the middle VO<sub>2</sub> switch with a period of 1 s and monitored the incubation time. The electrical excitation had a 20 ms time lag with respect to the heater signal (Fig. 3b). Therefore, in one electrical measurement, the VO<sub>2</sub> switch had a 20 ms relaxation time after a thermal IMT; in the next electrical measurement, the switch had a much longer relaxation time (1 s), which is considered to be the reference measurement (without memory). The results indicate that the thermally driven IMT also induces a change in incubation time (Fig. 3c). This suggests the generality of the effect, as well as the fact that the electric current in the film, which could induce excitation or movement of ions, does not play any role in the memory effect since there was no current flowing in the device during the thermally driven IMT.

VO<sub>2</sub> is an oxygen-rich thin film, and therefore, its junction with the top metal pads forms a metal–oxide interface that might exhibit non-volatile switching, as observed, for example, in TiO<sub>2</sub> (ref. <sup>18</sup>). In addition, metal atoms could potentially diffuse in the VO<sub>2</sub> film, resulting in persistent changes in the device. Nevertheless, our experiments showed that the metal–VO<sub>2</sub> junction plays no role in the observed memory for the following reasons. First, we found that the effect is independent of the metal type: Ti/Au (Fig. 1), Pt and Ti/Pt (Extended Data Fig. 2d,e). Second, we reproduced the memory effect in a cross structure (Fig. 3d), which enables triggering IMT only in the central portion of the VO<sub>2</sub> channel, without activating the metal–VO<sub>2</sub> interface. In this cross geometry, the vertical and horizontal directions (Fig. 3d, scanning electron microscopy (SEM) image) were independently excited, with two synchronized galvanically isolated sources. The vertical path was periodically triggered every 10 s, and the incubation time was monitored. Only for odd cycles (every 20 s), we activated the IMT in the horizontal direction, 1 s before triggering the vertical direction. We ensured that the

phase transition area due to triggering the IMT in the horizontal direction did not reach the vertical pads (Methods). The difference in the vertical incubation times in the odd (with 1 s memory) and even (reference) cycles shows that the memory originates from the VO<sub>2</sub> channel and not from the metal–VO<sub>2</sub> junction (Fig. 3e).

Post-IMT intermediate supercooled metallic domains<sup>19,20</sup> that can potentially persist considerably below the transition temperature are another possible mechanisms that could lead to memory effects in VO<sub>2</sub>. Electrical measurements have suggested that such metallic domains could persist up to a few milliseconds at temperatures below the IMT<sup>13</sup>. This was described by the classic metastability that generally exists in Mott systems with first-order transitions<sup>21</sup>. We performed measurements to understand whether long-lived metallic domains could play a role in our observations. Considering the very long timescales of our observed memory, one can use conventional microscopy techniques to monitor the lattice structures<sup>22</sup> or electronic properties<sup>23</sup> to directly reveal the possible existence of long-lived metallic domains in the film. Our Kelvin probe force microscopy measurements, however, did not show any signature of such domains, for scales greater than 30 nm at least (Extended Data Fig. 6).

We comprehensively explored the relation between long-lived metallic domains and our observations. The VO<sub>2</sub> cross experiment (Fig. 3d,e) shows that such possible long-lived metallic domains have to be in the VO<sub>2</sub> channel and not at the metal–VO<sub>2</sub> junction. In this case, one expects to see a more pronounced change in incubation time for devices with shorter channels, as the channel length approaches the size of the largest metallic domains. In the extreme case, where the channel size becomes shorter than the size of a metallic domain, the incubation time has to become zero. Such metallic domains are also expected to show a larger change in conductance in shorter channel devices, considering the film as a resistive network. The results presented in Fig. 3f show that devices with smaller channel lengths down to 50 nm exhibit a higher increase in conductance, which could be due to possible long-lived metallic domains that could persist in millisecond timescales<sup>13,24</sup>. The memory embedded in the incubation time, however, was nearly constant for all gap lengths (Fig. 3f and Extended Data Fig. 7). To say the least, these results show that the possible long-lived metallic domains should have dimensions notably below 50 nm.

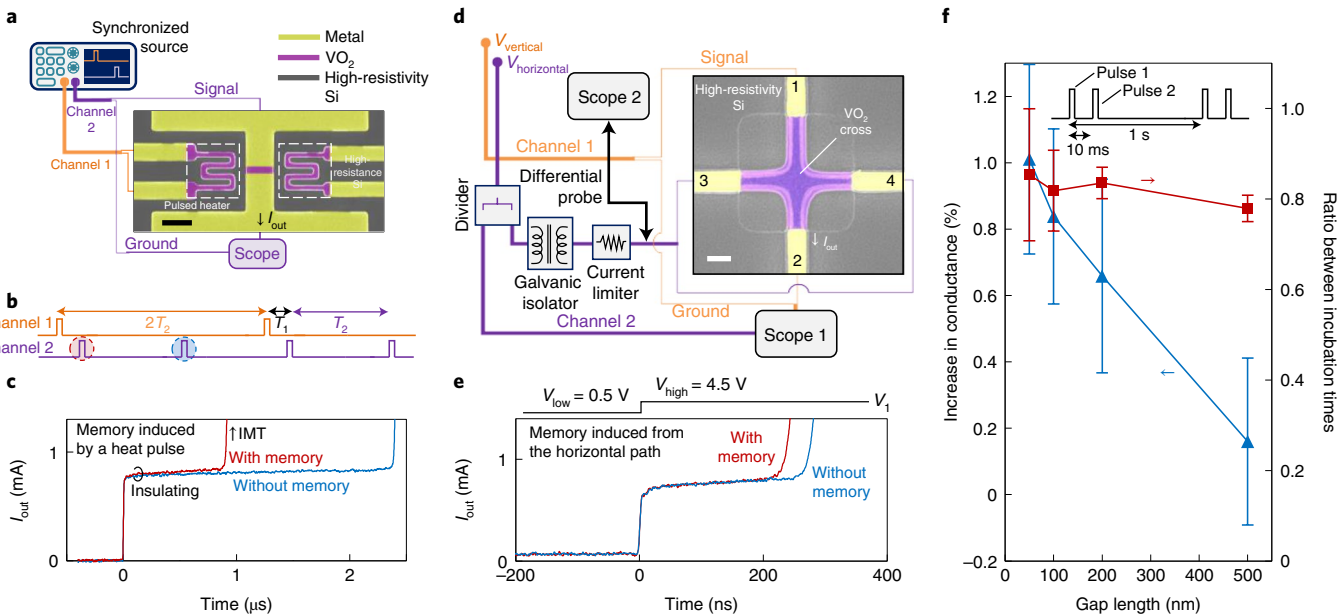


**Fig. 3 | Exploration on possible mechanisms behind the long memory.** **a**, Schematic of an experimental setup for a synchronized measurement in which the memory is induced by a heat pulse. **b**, Illustration of waveforms in the synchronized measurement. Channel 1 triggers the IMT in isolated pulsed heaters, which ensures thermal-driven phase transition in the middle switch. The effect of the heat-induced IMT is evaluated in the incubation of the middle switch excited by channel 2. **c**, Measurements indicate that memory can be induced by thermal IMT, showing the generality of the effect. **d**, Schematic of an experimental setup for a synchronized measurement on a  $\text{VO}_2$  cross structure. The effect of IMT triggering in the horizontal path is measured by monitoring the incubation time in the vertical path. Scale bar (false-coloured SEM image),  $2 \mu\text{m}$ . **e**, Output current at terminal 4 of the cross with a 1 s history of IMT triggered in the horizontal path (red) and without memory (blue). This indicates that the memory effect originates from the  $\text{VO}_2$  channel and rules out the possible effect from the metal- $\text{VO}_2$  junction. **f**, Evaluation of memory effect on  $\text{VO}_2$  devices with different gap lengths ranging from 50 to 500 nm. Although devices with smaller channel lengths show a higher increase in conductance, the memory embedded in the incubation time is nearly constant (Extended Data Fig. 7).

We also examined the IMT threshold voltage of the devices, which is known to be more sensitive to the presence of long-lived metallic domains than the channel resistance<sup>13</sup>. The results presented in Extended Data Fig. 8 show that the threshold voltage and resistance follow the same trend and totally relax after a few seconds, whereas the incubation time shows a logarithmic relaxation that keeps relaxing for orders of magnitude longer times. These measurements show that the incubation times are independent of threshold voltage and resistance changes. Although these results are not supportive of long-lived metallic domains as the main factor in our observation, due to the indirect nature of the performed measurements, they still do not totally rule out their possible contribution. Further studies such as those based on in situ high-resolution ultrafast microscopy techniques can provide a more conclusive picture.

### Structural glass-like features of the memory effect

We examined whether electronic states could be responsible for our observation. We evaluated the memory effect under continuous-wave (CW) laser pumping with relatively high-energy photons (2.33 eV), larger than the material bandgap<sup>25</sup>. The measurements under laser excitation show a considerably higher conductivity with respect to those under dark; however, the memory effect is not affected (Fig. 4a,b). This observation does not support scenarios that explain the memory effect based on the excitation of electronic states, such as orbital switching<sup>26</sup> or trapped carrier in defects. In fact, logarithmic or stretched exponential relaxations are fairly slow processes for electronic states; nevertheless, such long relaxation times are one of the main features of glassy states with configurational transitions<sup>27</sup>. The IMT in  $\text{VO}_2$  is an example of structural switching, and therefore, slow glass-like configurational changes driven by bond lengths, vacancies or possible long-lived metallic domains could be a possible explanation.

To investigate this possible scenario, we evaluated the memory effect at elevated temperatures to examine an important feature of glass-like relaxation: the system becomes more mobile close to the transition temperature<sup>28</sup>. In this case, an excitation signal can more easily perturb the system, and the system relaxes faster after removing the excitation. To examine this feature, we monitored the change in incubation times between periodic pulses with a separation of 1 s (reference pulses) and pulses with separations of 10 ms over a temperature sweep (Fig. 4a). At each temperature, we set the excitation amplitude to result in  $t_{\text{inc}} = 500 \text{ ns}$  for the reference pulse and monitored the incubation of the second pulse. We observed a much more pronounced change in incubation times close to the IMT (Fig. 4c,d). This difference in the incubation times is proportional to the slope of  $t_{\text{inc}}$  versus relaxation time (for example,  $78 \text{ ns dec}^{-1}$ ; Fig. 1c). Therefore, our results show faster relaxation at higher temperatures (Fig. 4c, inset), which is an important feature of glass-like systems. We note that in our ultrafast electrical measurements, the characterization of  $t_{\text{inc}}$  was limited to  $\sim 55^\circ\text{C}$  (Methods), and the trend of increasing the relaxation speed might not hold at the strong phase-coexistence regime<sup>29</sup>, where the metallic phase becomes metastable. The results presented elsewhere<sup>30</sup> showing  $\text{VO}_2$  relaxation by accurate resistance measurements might be connected to this behaviour: the relaxation rate is almost constant right at the beginning of the hysteresis region, and then it gets slower at the strong phase-coexistence regime.

Glass transitions are also reversible and can undergo new phase paths if they are re-excited before complete relaxation. These are analogous features of our observations (Fig. 1f and Fig. 2b). It should be noted that we obtained an identical memory effect under a vacuum of  $10^{-4} \text{ mbar}$ , which shows that such an off-stoichiometric mechanism must be purely configurational, without any exchange

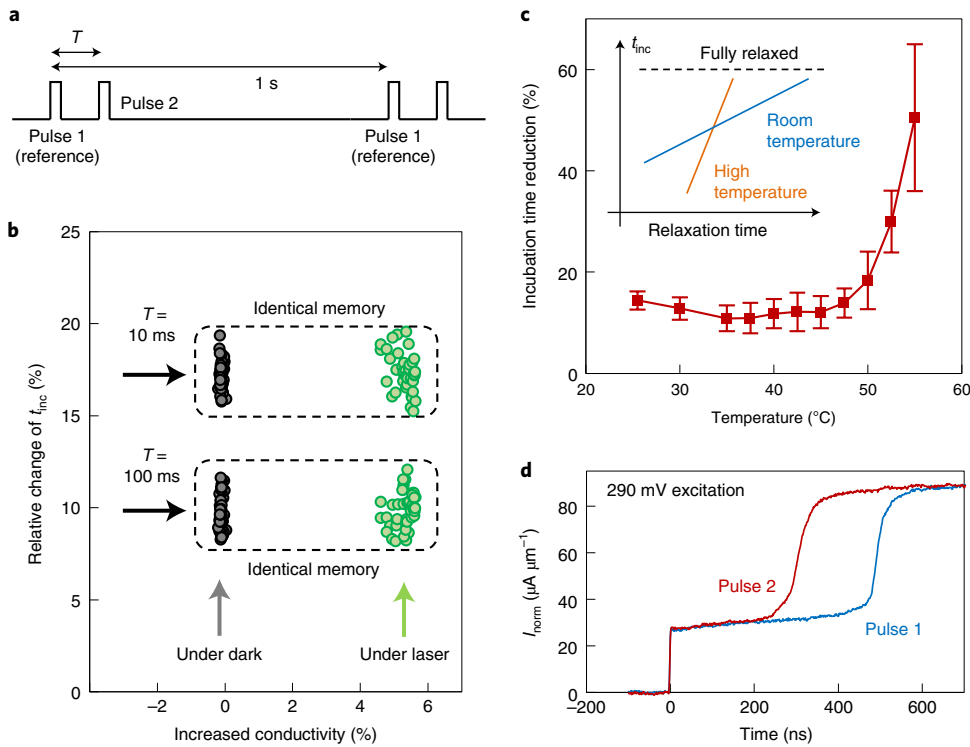


**Fig. 4 | Evidence of glass-like dynamics.** **a**, Illustration of the excitation signal of a VO<sub>2</sub> switch for measurements under laser light. Every second, two identical pulses with time separation  $T$  are applied to the device and incubation times are monitored ( $t_{\text{inc}}^{\text{ref}}$  and  $t_{\text{inc}}$ ). **b**, Relative change in the incubation time ( $(t_{\text{inc}} - t_{\text{inc}}^{\text{ref}})/t_{\text{inc}}^{\text{ref}}$ ) versus increased  $G_{\text{ins}}$  in a 200-nm-long channel VO<sub>2</sub> switch. Measurements under a CW 532 nm laser light with a power density of  $\sim 100 \text{ W cm}^{-2}$  show a considerably higher conductivity; however, the memory effect is unchanged. The experiment shows that the memory effect is likely structural. **c**, Relative change in incubation time after  $T=10 \text{ ms}$  with respect to the reference pulses with relaxation time of  $T=1 \text{ s}$  at different temperatures. The more pronounced change in  $t_{\text{inc}}$  at higher temperatures indicates faster relaxation (inset). **d**, Transient current density of the VO<sub>2</sub> switch corresponding to two consecutive triggering events with  $V_{\text{set}}=290 \text{ mV}$  at a chuck temperature of  $55^\circ\text{C}$ . The results show a notable change in  $t_{\text{inc}}$ .

with the ambience. Even though more investigations may be needed to comprehensively identify the microscopic details of this process, the observed effect certainly shares important features of glasses and thus can be considered as glass-like dynamics.

### Potential applications in computation and data storage

The concept of electrically accessible glass-like dynamics can offer opportunities in electronics. An important aspect of the observed effect is that at a constant amplitude,  $t_{\text{D}}$  is proportional to the energy required to activate the IMT. Therefore, the history of a device determines the switching energy barrier ( $E_{\text{bar}}$ ) in the future: the higher the number and frequency of switching events, the lower the energy barrier (Fig. 5a,b). One can model  $E_{\text{bar}}$  at  $t=t_0$  in the transient regime after  $n$  pulses occurring at  $t_k$  ( $1 \leq k \leq n$ ) by

$$E_{\text{bar}} = E_0 - E_1 \ln \left[ \sum_{k=1}^n \frac{T_0}{t_0 - t_k} \right], \quad (1)$$

where  $E_0$  is the energy barrier of the device (which is relaxed for  $T=T_0$ ) and  $E_1$  is a constant. The second term on the right-hand side of this equation represents the reduced energy barrier due to device history. Equation (1) captures the dynamic changes in  $t_{\text{inc}}$  both for uniform (Fig. 5a) and non-uniform (Extended Data Table 1) pulse patterns. This functionality can enable highly dynamic classifiers with computation-free training, which normally cannot be achieved in classic approaches based on nonlinear resistive elements<sup>31</sup>. To show this, we can consider a neural network with one hidden layer, in which a VO<sub>2</sub> switch is placed between each of the

two nodes (Fig. 5c). At time  $t$ , the network can be fully described by matrices  $E_{\text{bar}}^A(i, j, t)$  and  $E_{\text{bar}}^B(j, k, t)$  representing the reduced energy barrier of the  $A_i - X_j$  and  $X_j - B_k$  switches, respectively. The product of these two matrices corresponds to the correlation between inputs and outputs, enabling an energy-based classification: for each set of inputs, the output with the minimum energy required for triggering the IMT at the interconnections will be activated.

This concept provides two important features. First, training of the network can be done purely based on hardware. There is no need for the calculation of weights and also no need to physically induce them, for example, to manipulate the resistivity of elements<sup>31</sup>. We show this feature in classification of three characters, namely, 'T', 'J' and 'L' provided in  $3 \times 3$  pixels (Fig. 5d). The application of electric currents to the input nodes ( $A_i$ ) corresponding to each image label, and grounding the equivalent output, can simply train the network. For example, to train the network with sample 'J', the input nodes  $A_2$ ,  $A_4$ ,  $A_7$ ,  $A_8$  and  $A_9$  are activated and  $B_2$  is grounded, whereas all the other nodes are floating. This reduces the energy barrier for some of the pathways connecting each set of inputs to the corresponding output. Figure 5e illustrates the  $E_{\text{bar}}^A \times E_{\text{bar}}^B$  matrix with a colour map, representing the effective reduced energy barrier from the inputs to outputs. For example, in the case of sample 'J', the nodes  $A_2$ ,  $A_4$ ,  $A_7$ ,  $A_8$  and  $A_9$  have a lower energy barrier to fire IMTs towards output  $B_2$  (corresponds to 'J'). In this case, if one activates the abovementioned nodes, a higher current will be collected in node  $B_2$ . This approach yields a successful classification of the characters, as shown in the simulation results presented in Fig. 5f. The second feature provided by a glassy neural network is its self-tuning capability. The system is operational after initial training; however, it fine-tunes itself as it

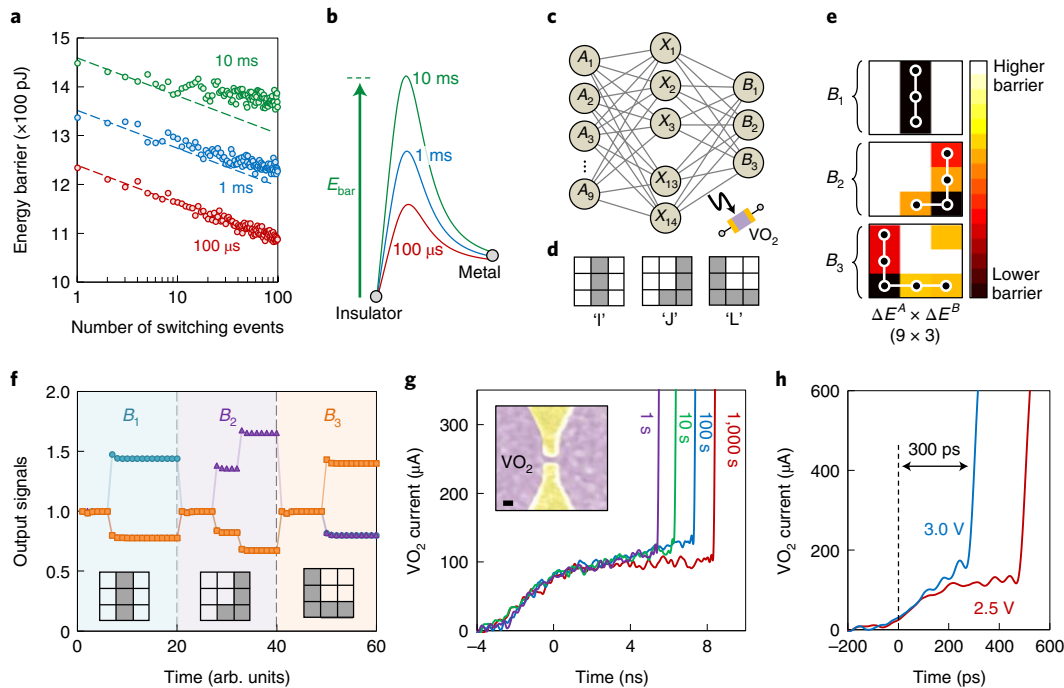


**Fig. 5 | Electrical control of glass-like dynamics for computation and data storage.** **a**, Dynamic change in energy barrier ( $E_{\text{bar}}$ ) of a 2- $\mu\text{m}$ -long  $\text{VO}_2$  switch with the number of switching events for different pulse separations. **b**, Schematic showing that shorter pulse separations result in lower  $E_{\text{bar}}$ . **c**, Considered neural network. A  $\text{VO}_2$  switch is placed in the interconnection between each of the two nodes.  $\Delta E^A$  and  $\Delta E^B$  matrices represent the reduced energy barriers corresponding to the  $A_i - X_j$  and  $X_j - B_k$  interconnections. **d**, Labels used to train a network for a  $3 \times 3$  pixel image classification. **e**, Post-training  $\Delta E^A \times \Delta E^B$  matrix represents the effective reduced energy barrier corresponding to each output. **f**, Simulated output signals at three nodes:  $B_1$  (circles),  $B_2$  (triangles) and  $B_3$  (squares). Exposing the network to the inputs and monitoring the output currents successfully classifies the samples. **g**, Measured current of a  $\text{VO}_2$  nanodevice showing the potential of glass-like relaxation for ultrascaled memory devices. The inset shows the false-coloured SEM image of the  $\text{VO}_2$  switch. Scale bar, 100 nm. **h**, Measured current of the  $\text{VO}_2$  nanodevice (inset of **g**) excited with  $V_{\text{set}} = 2.5\text{ V}$  (red line) and  $V_{\text{set}} = 3.0\text{ V}$  (blue line), showing that electrically induced memory can take place in the sub-nanosecond timescales.

is exposed to the unclassified samples, because each sample would induce switching events at the correct nodes, reducing their energy barriers. This can self-optimize the network during the classification process, only relying on a small training set.

The concept of electrically accessible glass-like states can also enable high-performance data-storage platforms (Extended Data Fig. 9). This is because the triggering process is fast, relaxation is fairly slow and manipulation capability enables storing multibits on a single physical bit. In addition, the memory effect can be accessed at very low voltages ( $\ll 500\text{ mV}$ ), which is beneficial for energy-efficient electronics<sup>32</sup> (Fig. 4d). Furthermore, the concept—relying on two-terminal devices—is compatible with a cross-bar configuration, which offers extremely high data-storage densities<sup>33</sup>. Figure 5g shows a  $50\text{ nm} \times 200\text{ nm}$   $\text{VO}_2$  nanoswitch, in which the device history can be read in sub-10 ns. The writing process (triggering the IMT that induces the memory) can take place in sub-nanosecond timescales with a low energy cost of  $\sim 100\text{ fJ}$  (Fig. 5h). We note that a considerable portion of the measured current in the device (Fig. 5g inset) is from the fringing current that can be eliminated by defining a mesa region around the device. Therefore, the writing energy cost can go well below 100 fJ.

We also add that the demonstration of memory effect in four-terminal cross structures open possibilities in implementations for computational and memory devices. For neural networks, the vertical direction (Fig. 3d) can be considered as the signal propagation path and the device can be programmed through independent horizontal terminals. For memory devices, this four-terminal configuration enables the reading and writing process to take place from different ports.

## Conclusions

We have reported glass-like dynamics in  $\text{VO}_2$  that can be excited in sub-nanosecond timescales and monitored for several orders of magnitudes in time, from microseconds to hours. A two-terminal switch undergoes complex but predictable and reversible dynamics, induced by a series of excitations. From a technological point of view, our results show that the response of these dynamics to a sequence of excitations can enable new schemes for data storage and processing. Our functional devices can, thus, potentially meet the continuous demands of electronics in terms of downscaling<sup>33</sup>, fast operation<sup>34</sup> and decreasing the voltage-supply level<sup>32,35</sup>. From a physical point of view, our work reveals extremely long memories in  $\text{VO}_2$  that can only be revealed by the incubation time. Monitoring incubation times to measure a sensitive nanoscale lattice and electronic phases could also be used to study out-of-equilibrium phase dynamics in other material systems<sup>36,37</sup>.

## Methods

**General.** All the measurements have been done under controlled ambient conditions ( $21.5 \pm 0.5^\circ\text{C}$ ), unless otherwise stated in the manuscript. All the represented error bars indicate the standard deviation ( $\pm \sigma$ ).

**Sputtered film deposition on high-resistivity Si substrates.** The sputtered polycrystalline  $\text{VO}_2$  film was 100 nm thick and deposited on a high-resistivity Si substrate. A vanadium target (99.95% pure) was used in a plasma chamber with a pressure of 0.007 mbar, oxygen flow of 22.1 s.c.c.m. and argon flow of 12.5 s.c.c.m. The substrate temperature was 600 °C during deposition.

**Synthesis of epitaxial  $\text{VO}_2$  on  $\text{Al}_2\text{O}_3$  and  $\text{TiO}_2$  substrates.** The  $\text{VO}_2$  films were grown on the (001)  $\text{TiO}_2$  and (0001)  $\text{Al}_2\text{O}_3$  substrates by PLD. For fabricating the ceramic target for growing stoichiometric  $\text{VO}_2$  films, stoichiometric  $\text{V}_2\text{O}_5$  (99.99%,

Sigma-Aldrich) powder was sintered at 600 °C for 18 h. The (001) TiO<sub>2</sub> and (0001) Al<sub>2</sub>O<sub>3</sub> substrates were loaded into a high-vacuum PLD chamber and evacuated to a base pressure of  $\sim 1 \times 10^{-6}$  torr. Then, the prepared V<sub>2</sub>O<sub>5</sub> ceramic target was ablated by focusing the KrF excimer laser ( $\lambda = 248$  nm) at a laser fluence of 1 J cm<sup>-2</sup> and laser frequency of 1 Hz. V<sub>2</sub>O<sub>5</sub> films were grown on the (001) TiO<sub>2</sub> substrates at substrate temperature ( $T_g$ ) of  $\sim 300$  °C with oxygen partial pressure ( $p_{O_2}$ ) of 18 mtorr and on the (0001) Al<sub>2</sub>O<sub>3</sub> substrates at  $T_g \approx 450$  °C with  $p_{O_2} \approx 30$  mtorr. After growth, both samples were cooled down to room temperature at 20 °C min<sup>-1</sup>. Symmetric  $2\theta - \omega$  scans (2θ is the diffracted angle, defined between detector angle and incident beam, and  $\omega$  represents the incident angle, defined between X-ray source and the sample) were performed by using a high-resolution X-ray diffractometer (D8 Discover, Bruker;  $\lambda = 0.15406$  nm) at the Materials Imaging & Analysis Center of POSTECH (Pohang). Also, temperature-dependent sheet resistance during heating and cooling cycles was measured at the van der Pauw geometry by using a Hall measurement system.

**Fabrication of VO<sub>2</sub> switches with micrometre-range gap distances.** After VO<sub>2</sub> film synthesis and dicing the samples into 1 cm × 1 cm chips, the fabrication process was followed by electron-beam physical vapour deposition. Different metallic layers (Ti/Au, Ti/Pt and Pt) were used, all with 200 nm thickness. In case of using Ti as the adhesion layer, the corresponding thickness was 10 nm. The gap was defined using a lithography step with 375 nm laser (AZ nLOF 2020 photoresist), followed by ion-beam etching. Then, the definition of pads and mesa was performed, using the same lithography and etching technique.

**Fabrication of VO<sub>2</sub> nanoswitches.** For nanodevice fabrication on VO<sub>2</sub> on sapphire, the process was started by metal deposition (1 nm Cr/40 nm Au/1 nm Cr). Then, an electron-beam lithography step with a 50% ZEP resist (a styrene methyl acrylate-based positive electron-beam resist baked at 180 °C) followed by ion-beam etching was employed to form the nanogaps and radio-frequency pads.

**High-bandwidth large-signal measurement.** High-frequency electrical measurements are typically performed in the frequency domain, where the device under test is characterized based on scattering matrix parameters. This method, however, is not able to capture large-signal switching transients. Instead, we used a time-domain measurement technique, where the device is excited by a pulse generator with 3 ns rise time, and switching transient of the VO<sub>2</sub> device is measured with an ultrahigh-speed oscilloscope with a DPO70000SX 70 GHz Tektronix oscilloscope. To achieve an extremely precise measurement, we used radio-frequency probes with the ground–signal–ground configuration, which provide 67 GHz bandwidth. The voltage waveform at the 50 Ω port of the oscilloscope were measured. Dividing the measured voltage by 50 Ω yields the current flowing through the VO<sub>2</sub> film.

**Thermal measurements.** Thermal measurements were performed using a Quantum Focus Instrument infrared microscope with a 512 × 512 pixel InSb infrared detector array cooled using liquid nitrogen. This setup is equipped with lenses and filters providing 20-fold optical magnification, high resolution (~2.8 μm) and accuracy. An active thermal stage with a thermoelectric module, a forced-convection heat sink and a precise temperature controller enabled an accurate emissivity correction using the factory-provided calibration data. In addition, to increase the emissivity of the chips and to avoid errors due to the infrared transparency of the layers, black paint was used on top of the chips. For all the measurement points in this work, accurate pixel-by-pixel emissivity calibrations were performed to ensure valid measurements. The transient temperature measurements were limited to a frame rate of 26.71 fps due to processing and data transfer delays between the module and computer.

**Measurements on VO<sub>2</sub> crosses.** We used a transformer to isolate the vertical and horizontal excitations of the VO<sub>2</sub> cross (Fig. 3d). In this case, no net charge transfer is possible between terminals 1 and 2 and terminals 3 and 4, since the horizontal and vertical signals do not share the ground. To make sure that IMT takes place in the horizontal direction, we measured the voltage signal after the transformer with a 1 GHz differential probe (which does not impose the global ground to terminals 3 and 4).

The vertical direction was terminated by the 50 Ω port of a 70 GHz scope, which limited the current passing through terminals 1 and 2. To limit the current in the horizontal direction, we used an off-chip 100 Ω resistor. We always supplied a 500 mV d.c. voltage (Fig. 3e,  $V_{low}$ ) to terminal 1 and monitored the vertical current flow at terminal 4 (Fig. 3e; the current is non-zero for  $t < 0$ ). This is to make sure that the phase transition area due to triggering the horizontal path does not reach the vertical pads. Therefore, the observed memory effect in the vertical direction is solely due to exciting the VO<sub>2</sub> channel and not the metal–VO<sub>2</sub> junction.

**High-temperature ultrafast measurements.** As shown in the schematic of the experimental setup (Fig. 1a), ultrafast electrical measurements were done in a two-port configuration, in which both function generator and oscilloscope have 50 Ω terminations, which is necessary for precise high-bandwidth measurements. At the same time, these 50 Ω terminations limit the current passing through the

device, especially when VO<sub>2</sub> is in the metallic state. This a beneficial aspect because it avoids overheating and damaging the device, which enables degradation-free operation (Extended Data Fig. 2c).

For high-temperature measurements, the resistance of the off state becomes considerably lower, getting close to the resistance of the metallic phase. This results in a rather small on/off ratio. In this case, the 50 Ω series resistances dominate both on-state and off-state resistances, and insulator–metal switching was not detectable. Therefore, the characterization of relaxation time at the strong phase-coexistence regime ( $T > 55$  °C; Extended Data Fig. 2b) was not possible with our ultrafast technique.

**Multilevel ultrascaled memory.** The results reported in Fig. 2 present a multilevel memory concept, in which the information is stored in nanoscale atomic/molecular configurations, as an alternative to charge-based memory devices. This can be realized by two-port switches with nanogaps, which have the potential capability to be implemented in a cross-bar configuration resulting in extremely high densities. Figure 5g shows the switching transient of a 50-nm-long gap VO<sub>2</sub> switch for different values of relaxation times. Nanodevices exhibit a similar memory effect in much shorter incubation times, which enables a reading time below 10 ns. Figure 5h shows that triggering the IMT in a nanodevice by an over-threshold pulse can be even much faster than 10 ns (well below 1 ns) with an energy consumption in the range of 0.1 pJ. This enables a sub-nanosecond writing process. Extended Data Fig. 9a illustrates a potential implementation of a multilevel Mott-based memory, which includes three reference bits ( $R_1$ ,  $R_2$  and  $R_3$ ) together with a row of data bits ( $B_k$ ,  $1 < k < n$ ). Each bit corresponds to a two-port VO<sub>2</sub> switch. For writing a row of bits, the three reference bits are correspondingly written with  $N_1$ ,  $N_2$  and  $N_3$  pulses. Applying different number of pulses to each bit  $B_k$  induces four distinct states expressed as  $N_1$ ,  $N_2$ ,  $N_3$  or nothing. For reading, the first reference bit is initially submitted to a series of pulses with increasing widths, until the IMT is triggered (Extended Data Fig. 9b). This indicates the pulse width  $W_k$  required to trigger the IMT in those bits that were written with  $N_k$  pulses. We call this the key pulse corresponding to the reference bit  $R_k$  (Extended Data Fig. 9c). Then, key pulses 1, 2 and 3 are applied to the data bits (Extended Data Fig. 9d), and the first pulse that triggers the IMT determines the written data. If none of the pulses trigger the IMT, it has not been written. The scheme relies only on a fixed amplitude by changing the pulse width, which is straightforward in electronics.

**Validation of the empirical equation of  $E_{bar}$  in a non-uniform pattern.** We examined the accuracy of equation (1) in a non-uniform pattern of pulses with the following separations: 1 s, 10 ms, 1 ms, 100 ms, 1 ms, 1 ms, 1 ms. We periodically repeated this pattern and measured the corresponding incubation times.

Equation (1) represents the energy barrier after  $n$  switching events. The equation can be equivalently written for the incubation times:

$$t_{inc} = t_{inc,0} - t_1 \ln \left( \sum_{k=1}^n \frac{T_0}{t_0 - t_k} \right), \quad (2)$$

where  $t_{inc,0}$  represents the incubation time of the switch relaxed for  $T = T_0$  after  $n$  excitations. In this case, we consider the pulse after the longest relaxation ( $T_0 = 1$  s) as the reference pulse (with incubation time  $t_{inc,0}$ ). Using equation (2), we write the reduced incubation time of each pulse with respect to the reference pulse.

$$t_{inc,0} - t_{inc}^{pulse 1} = t_1 \log \left( \frac{1}{0.01} \right) = 2t_1 \quad (3.1)$$

$$t_{inc,0} - t_{inc}^{pulse 2} = t_1 \log \left( \frac{1}{0.001} + \frac{1}{0.011} \right) = 3.038t_1 \quad (3.2)$$

$$t_{inc,0} - t_{inc}^{pulse 3} = t_1 \log \left( \frac{1}{0.1} + \frac{1}{0.101} + \frac{1}{0.111} \right) = 1.461t_1 \quad (3.3)$$

$$t_{inc,0} - t_{inc}^{pulse 4} = t_1 \log \left( \frac{1}{0.001} + \frac{1}{0.101} + \frac{1}{0.102} + \frac{1}{0.112} \right) = 3.012t_1 \quad (3.4)$$

$$t_{inc,0} - t_{inc}^{pulse 5} = t_1 \log \left( \frac{1}{0.001} + \frac{1}{0.002} + \frac{1}{0.102} + \frac{1}{0.103} + \frac{1}{0.113} \right) = 3.184t_1 \quad (3.5)$$

$$\begin{aligned} t_{inc,0} - t_{inc}^{pulse 6} \\ = t_1 \log \left( \frac{1}{0.001} + \frac{1}{0.002} + \frac{1}{0.003} + \frac{1}{0.103} + \frac{1}{0.104} + \frac{1}{0.114} \right) = 3.27t_1 \end{aligned} \quad (3.6)$$

Based on these calculations, the only parameter describing the transient change in the incubation times is  $t_1$ , which is equal to the change in incubation time by one decade change in relaxation time. Using  $t_1 = 68.5$  ns, we have the values reported

in Extended Data Table 1, which show excellent agreement with the measurement results.

## Data availability

All the data supporting the claims of this paper are available from the corresponding authors upon reasonable request.

Received: 28 February 2022; Accepted: 12 July 2022;

Published online: 22 August 2022

## References

- Dagotto, E. Complexity in strongly correlated electronic systems. *Science* **309**, 257–262 (2005).
- Shao, Z. W., Cao, X., Luo, H. & Jin, J. P. Recent progress in the phase-transition mechanism and modulation of vanadium dioxide materials. *NPG Asia Mater.* **10**, 581–605 (2018).
- Oh, S. et al. Energy-efficient Mott activation neuron for full-hardware implementation of neural networks. *Nat. Nanotechnol.* **16**, 680–687 (2021).
- Bohaičuk, S. M. et al. Fast spiking of a Mott VO<sub>2</sub>-carbon nanotube composite device. *Nano Lett.* **19**, 6751–6755 (2019).
- Briggs, R. M., Pryce, I. M. & Atwater, H. A. Compact silicon photonic waveguide modulator based on the vanadium dioxide metal-insulator phase transition. *Opt. Express* **18**, 11192–11201 (2010).
- Strelcov, E., Lilach, Y. & Kolmakov, A. Gas sensor based on metal-insulator transition in VO<sub>2</sub> nanowire thermistor. *Nano Lett.* **9**, 2322–2326 (2009).
- Evert, V. The metal-insulator transitions of VO<sub>2</sub>: a band theoretical approach. *Ann. Phys.* **514**, 650–702 (2002).
- del Valle, J. et al. Spatiotemporal characterization of the field-induced insulator-to-metal transition. *Science* **373**, 907–911 (2021).
- Nakano, M. et al. Collective bulk carrier delocalization driven by electrostatic surface charge accumulation. *Nature* **487**, 459–462 (2012).
- Shukla, N. et al. A steep-slope transistor based on abrupt electronic phase transition. *Nat. Commun.* **6**, 7812 (2015).
- Liu, M. et al. Terahertz-field-induced insulator-to-metal transition in vanadium dioxide metamaterial. *Nature* **487**, 345–348 (2012).
- Gao, X., Rosário, C. M. M. & Hilgenkamp, H. Multi-level operation in VO<sub>2</sub>-based resistive switching devices. *AIP Adv.* **12**, 015218 (2022).
- del Valle, J. et al. Subthreshold firing in Mott nanodevices. *Nature* **569**, 388–392 (2019).
- Fisher, B., Patlagon, L. & Reisner, G. M. Sliding twin-domains in self-heated needle-like VO<sub>2</sub> single crystals. *Sci. Rep.* **10**, 6833 (2020).
- del Valle, J. et al. Generation of tunable stochastic sequences using the insulator–metal transition. *Nano Lett.* **22**, 1251–1256 (2022).
- Samizadeh Nikoo, M. et al. Nanoplasma-enabled picosecond switches for ultrafast electronics. *Nature* **579**, 534–539 (2020).
- Shabalin, A. G. et al. Nanoscale imaging and control of volatile and non-volatile resistive switching in VO<sub>2</sub>. *Small* **16**, 2005439 (2020).
- Strukov, D. B., Snider, G. S., Stewart, D. R. & Williams, R. S. The missing memristor found. *Nature* **453**, 80–83 (2008).
- Wei, J., Wang, Z., Chen, W. & Cobden, D. H. New aspects of the metal–insulator transition in single-domain vanadium dioxide nanobeams. *Nat. Nanotechnol.* **4**, 420–424 (2009).
- Ramírez, J. G., Sharoni, A., Dubi, Y., Gómez, M. E. & Schuller, I. K. First-order reversal curve measurements of the metal–insulator transition in VO<sub>2</sub>: signatures of persistent metallic domains. *Phys. Rev. B* **79**, 235110 (2009).
- Abreu, E. et al. Nucleation and growth bottleneck in the conductivity recovery dynamics of nickelate ultrathin films. *Nano Lett.* **20**, 7422 (2020).
- Cheng, S. et al. Inherent stochasticity during insulator–metal transition in VO<sub>2</sub>. *Proc. Natl Acad. Sci. USA* **118**, e2105895118 (2021).
- Sohn, A., Kanki, T., Sakai, K., Tanaka, H. & Kim, D.-W. Fractal nature of metallic and insulating domain configurations in a VO<sub>2</sub> thin film revealed by Kelvin probe force microscopy. *Sci. Rep.* **5**, 10417 (2015).
- Vaskivskyi, I. et al. Controlling the metal to insulator relaxation of the metastable hidden quantum state in 1T-TaS<sub>2</sub>. *Sci. Adv.* **1**, e1500168 (2015).
- Lee, S. et al. Electronic structure and insulating gap in epitaxial VO<sub>2</sub> polymorphs. *Appl. Mater.* **3**, 126109 (2015).
- He, Z. & Millis, A. J. Photoinduced phase transitions in narrow-gap Mott insulators: the case of VO<sub>2</sub>. *Phys. Rev. B* **93**, 115126 (2016).
- Palmer, R. G., Stein, D. L., Abrahams, E. & Anderson, P. W. Models of hierarchically constrained dynamics for glassy relaxation. *Phys. Rev. Lett.* **53**, 958–961 (1984).
- Heckshera, T. et al. Toward broadband mechanical spectroscopy. *Proc. Natl. Acad. Sci. USA* **114**, 8710–8715 (2017).
- Qazilbash, M. M. et al. Mott transition in VO<sub>2</sub> revealed by infrared spectroscopy and nano-imaging. *Science* **318**, 1750–1753 (2007).
- Claassen, J. H., Lu, J. W., West, K. G. & Wolf, S. A. Relaxation dynamics of the metal–semiconductor transition in VO<sub>2</sub> thin films. *Appl. Phys. Lett.* **96**, 132102 (2010).
- Prezioso, M. et al. Training and operation of an integrated neuromorphic network based on metal-oxide memristors. *Nature* **521**, 61–64 (2015).
- Ionescu, A. M. & Riel, H. Tunnel field-effect transistors as energy-efficient electronic switches. *Nature* **479**, 329–337 (2011).
- Pi, S. et al. Memristor crossbar arrays with 6-nm half-pitch and 2-nm critical dimension. *Nat. Nanotechnol.* **14**, 35–39 (2019).
- Wang, P. F. et al. A semi-floating gate transistor for low-voltage ultrafast memory and sensing operation. *Science* **341**, 640–643 (2013).
- Manca, N. et al. Selective high-frequency mechanical actuation driven by the VO<sub>2</sub> electronic instability. *Adv. Mater.* **29**, 1701618 (2017).
- Hollander, M. J. et al. Electrically driven reversible insulator–metal phase transition in 1T-TaS<sub>2</sub>. *Nano Lett.* **15**, 1861–1866 (2015).
- Grimaldi, E. et al. Single-shot dynamics of spin-orbit torque and spin-transfer torque switching in three-terminal magnetic tunnel junctions. *Nat. Nanotechnol.* **15**, 111–117 (2020).
- Yang, J. J., Strukov, D. B. & Stewart, D. R. Memristive devices for computing. *Nat. Nanotechnol.* **8**, 13–24 (2013).

## Acknowledgements

We are grateful to the help of the staff at the Center of Micro and Nano Technology (CMi) at EPFL with the fabrication process. We thank A. Ionescu for discussions. Y.P. and J.S. acknowledge support for the PLD growth from the Basic Science Research Program (2020R1A4A1018935) through the National Research Foundation of Korea (NRF) funded by the Ministry of Science and ICT.

## Author contributions

M.S.N. and E.M. conceived the project. M.S.N., E.M. and P.J.W.M. proposed the mechanism hypothesis. A. Krammer, Y.P., A.S. and J.S. synthesized the VO<sub>2</sub> films. M.S.N. fabricated the devices and performed and analysed the electrical measurements. R.S. performed and analysed the thermal microscopy measurements. G.M.M. and A. Kis performed and analysed the Kelvin probe force microscopy measurements. M.S.N. and E.M. wrote the manuscript with input from all the authors.

## Competing interests

The authors declare no competing interests.

## Additional information

**Extended data** is available for this paper at <https://doi.org/10.1038/s41928-022-00812-z>.

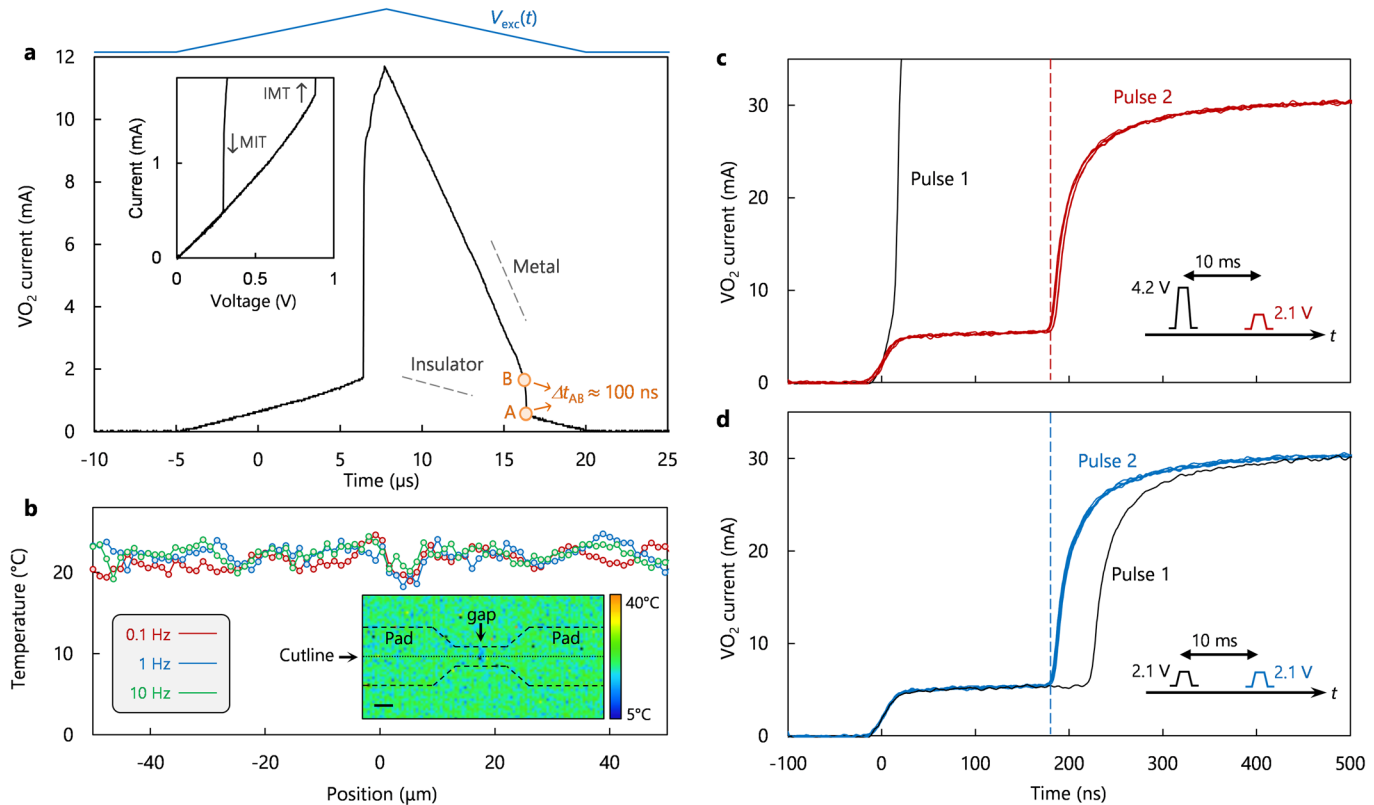
**Correspondence and requests for materials** should be addressed to Mohammad Samizadeh Nikoo or Elison Matioli.

**Peer review information** *Nature Electronics* thanks the anonymous reviewers for their contribution to the peer review of this work.

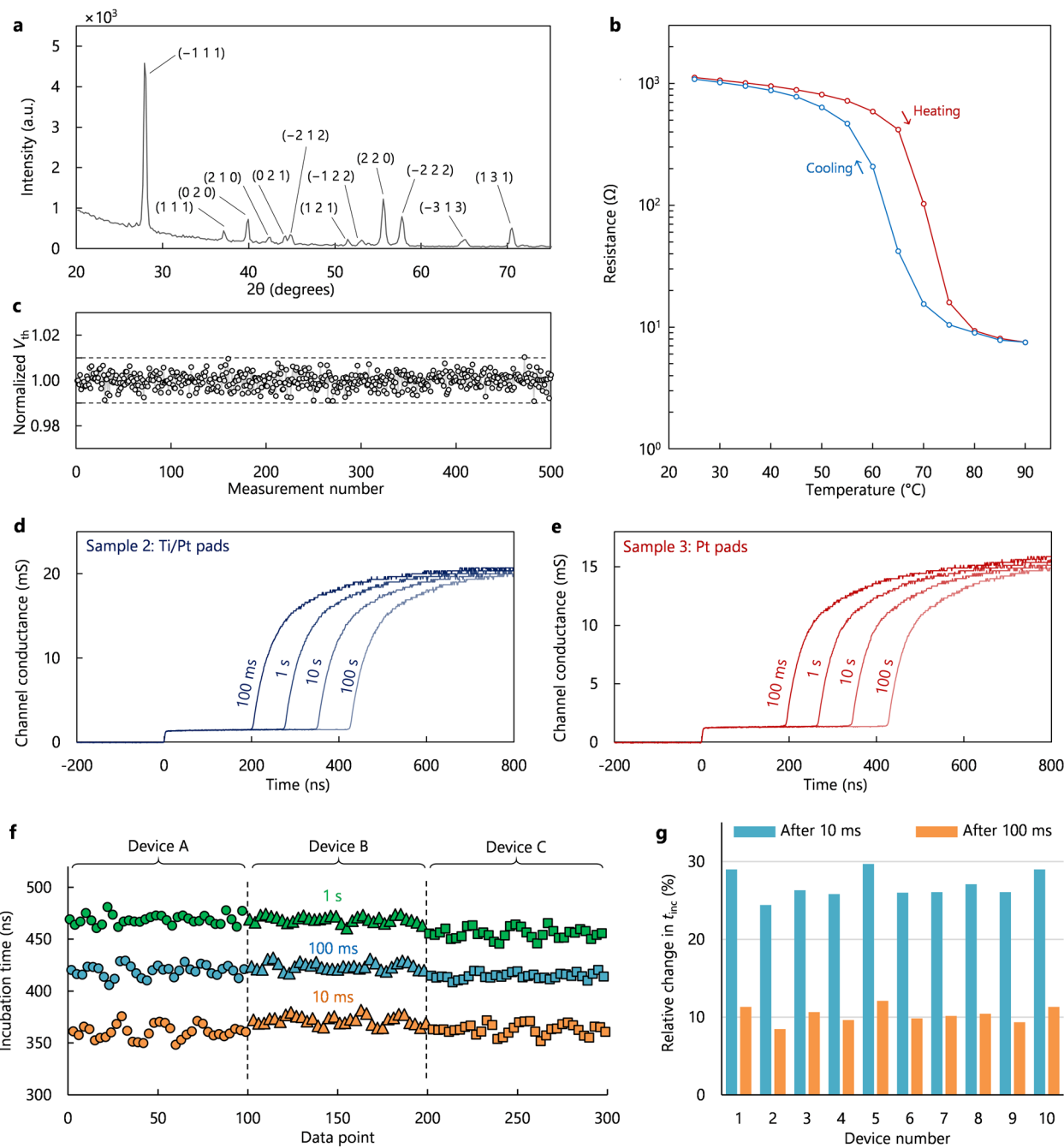
**Reprints and permissions information** is available at [www.nature.com/reprints](http://www.nature.com/reprints).

**Publisher's note** Springer Nature remains neutral with regard to jurisdictional claims in published maps and institutional affiliations.

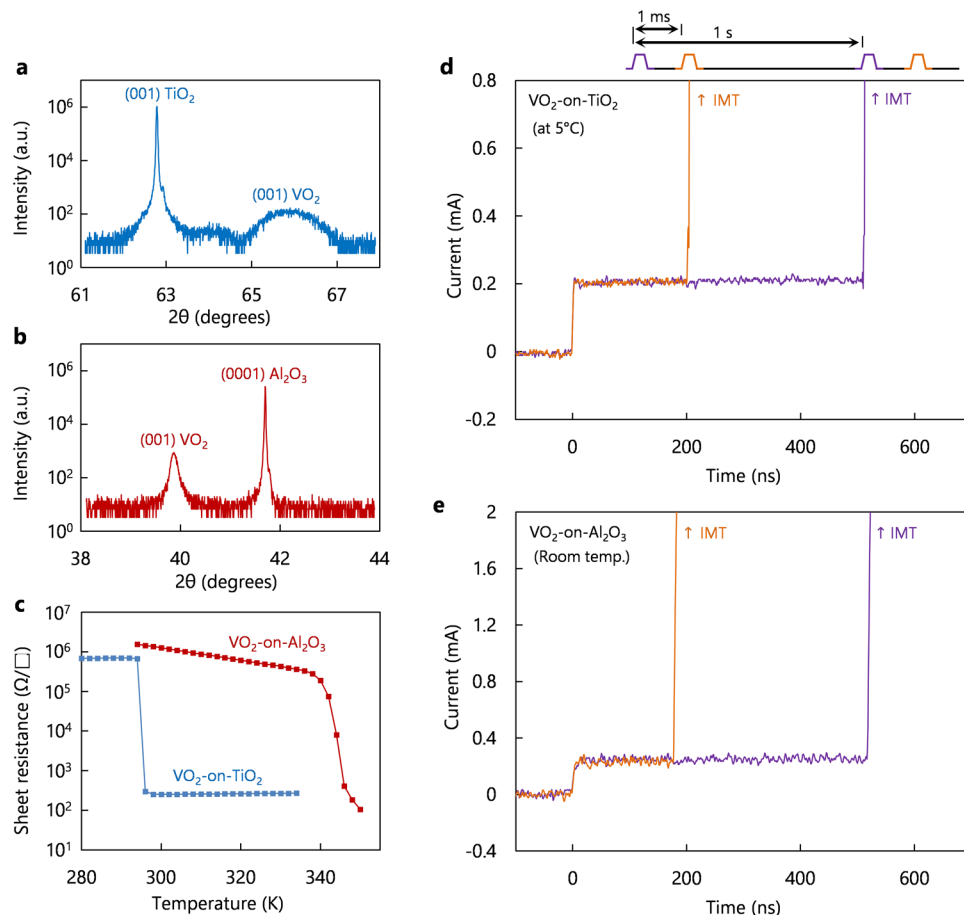
© The Author(s), under exclusive licence to Springer Nature Limited 2022



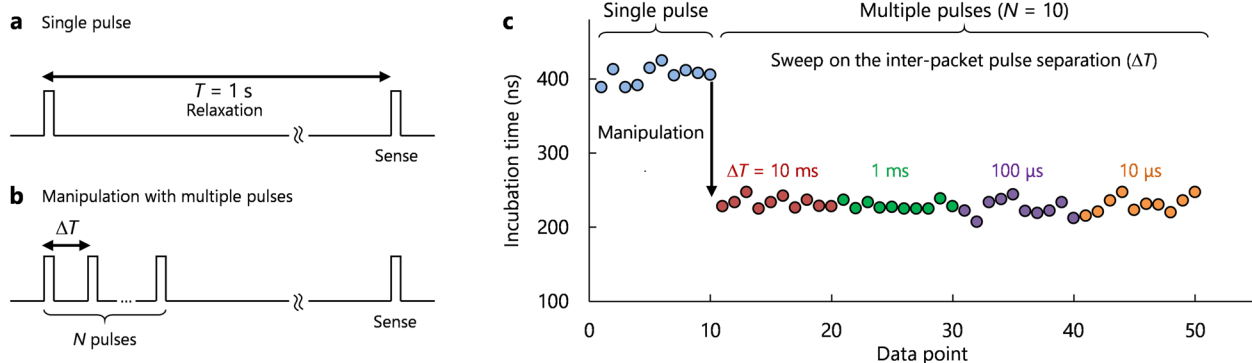
**Extended Data Fig. 1 | Investigation on the possible effect of temperature rise on the observed memory effect.** **a**, Measured current of a  $\text{VO}_2$  switch under triangular excitation. The MIT happens between points A and B with a short time separation of  $\Delta t_{AB} \approx 100 \text{ ns}$ . The inset presents the extracted resistance of the device in the IMT and MIT cycles showing that post excitation resistance is close (within 1%) to the pre-IMT resistance. This is another indication of the fast sub-microsecond cooling. **b**, Thermal microscopy of a two-terminal  $\text{VO}_2$  switch triggered by 10- $\mu\text{s}$  pulses ( $V_{\text{set}} = 2.1 \text{ V}$ ) with three different frequencies 0.1 Hz, 1 Hz and 10 Hz. The captured average temperature over the device does not show any notable difference between the three cases. This indicates that given the long time duration of our observed memory, this memory effect cannot be originated from thermal effects. **c,d**, Investigation of the memory effect for different excitation amplitudes  $V_{\text{set}} = 4.2 \text{ V}$  and  $2.1 \text{ V}$ , respectively. If thermal effects induced the memory effect, then the 4.2 V excitation should result in a more pronounced change in the incubation time, because it leads to a higher temperature rise comparing to 2.1 V excitation. The measured incubation times, however, are identical, which disproves the role of thermal effects in our observed memory.



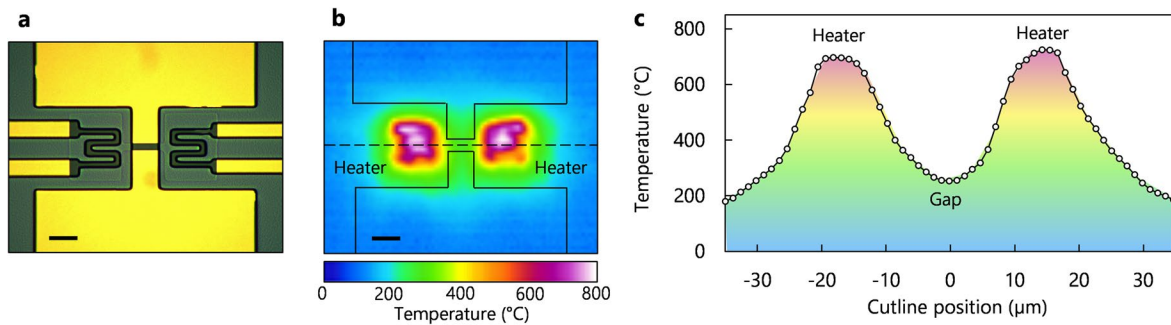
**Extended Data Fig. 2 | Evaluation of Vanadium Dioxide film and fabricated devices.** **a**, The  $\theta - 2\theta$  X-ray diffraction (XRD) pattern, recorded in the  $20^\circ - 75^\circ$  ( $2\theta$ ) range. The result indicates that the sample is crystallized in the single monoclinic phase as all diffraction peaks are indexed to monoclinic  $\text{VO}_2$  (M1) crystal structure according to PDF 04-003-4401 (Space group P2<sub>1</sub>/c,  $a = 5.75 \text{ \AA}$ ,  $b = 4.52 \text{ \AA}$ ,  $c = 5.38 \text{ \AA}$ ,  $\beta = 122.6^\circ$ ). **b**, Resistance versus temperature of a two-port  $\text{VO}_2$  switch. **c**, Threshold consistency indicating no degradation in a 3- $\mu\text{m}$ -long  $\text{VO}_2$  switch. **d,e**, Reproducibility of the results in devices with other metallic pads. Two-port switches fabricated on the high resistivity silicon substrate, based on  $\text{VO}_2 / \text{Ti} (10 \text{ nm}) / \text{Pt} (200 \text{ nm})$  and  $\text{VO}_2 / \text{Pt} (200 \text{ nm})$  structures, exhibit identical memory behavior. **f**, Measured incubation times over 100 consecutive measurements for three devices with identical geometries with 500-nm-long channels. **g**, Consistency of the memory effect defined as  $m = t_{inc}^{\text{ref}} / t_{inc} - 1$  for ten devices with the same geometry.  $t_{inc}^{\text{ref}}$  is the incubation of the reference pulse (corresponding to 1 second relaxation), and  $t_{inc}$  represents the incubation time corresponding to pulses with 10 ms (blue columns) or 100 ms (orange columns) relaxation times.



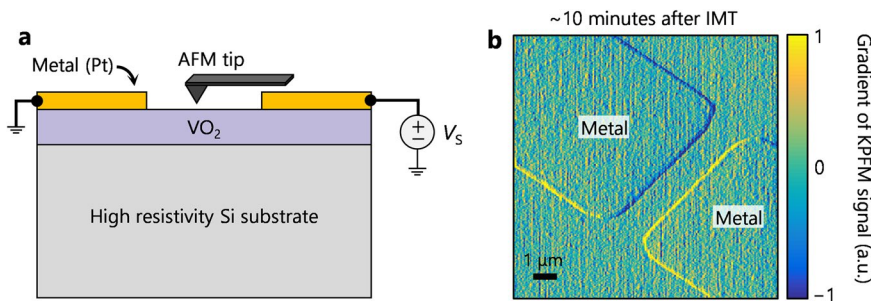
**Extended Data Fig. 3 | Reproducibility of the results on a single-crystal  $\text{VO}_2$  samples on  $\text{TiO}_2$  and  $\text{Al}_2\text{O}_3$  substrates.** Symmetrical 20- $\theta$  XRD scan on the **a**, 10 nm-thick  $\text{VO}_2$  film grown on (001)  $\text{TiO}_2$  substrate ( $\text{VO}_2\text{-on-}\text{TiO}_2$ ), and **b**, 100 nm thick  $\text{VO}_2$  film grown on (0001)  $\text{Al}_2\text{O}_3$  ( $\text{VO}_2\text{-on-}\text{Al}_2\text{O}_3$ ). **c**, Sheet resistance measurements on  $\text{VO}_2\text{-on-}\text{TiO}_2$  and  $\text{VO}_2\text{-on-}\text{Al}_2\text{O}_3$  samples in the heating cycle. In case of  $\text{VO}_2$  grown on the (001)  $\text{TiO}_2$  substrate, which is strained along the c-axis by -1.2%, the transition temperature is shifted from ~340 K to ~292 K. **d,e**, Pulsed-measurements with two relaxation times - 1-ms and 1-s - on  $\text{VO}_2\text{-on-}\text{TiO}_2$  and  $\text{VO}_2\text{-on-}\text{Al}_2\text{O}_3$  samples, showing the strong dependence of  $t_{\text{inc}}$  on the relaxation time. In case of the  $\text{VO}_2\text{-on-}\text{TiO}_2$  sample, the stage temperature was 5 °C to ensure that the film reverts back to the insulating state after removing the excitation.



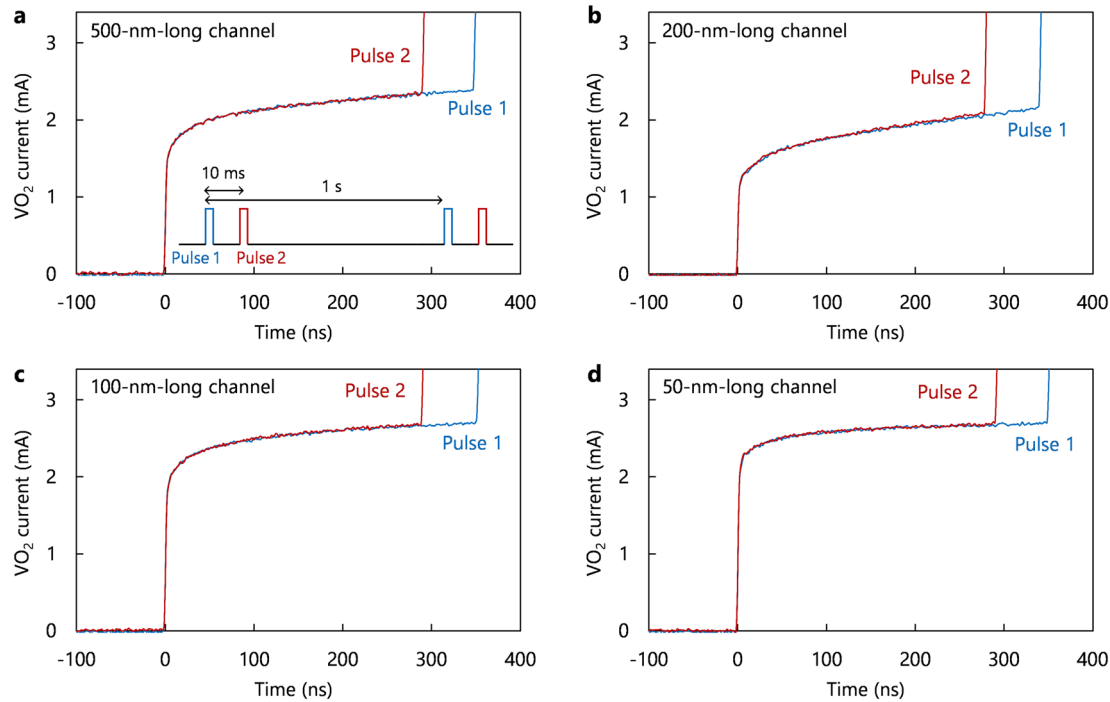
**Extended Data Fig. 4 | Effect of inter-packet pulse separation on manipulation of the device state.** **a**, Schematic of a waveform corresponding to a single-pulse excitation ( $V_{\text{set}} = 2.7\text{ V}$  and  $1\text{-}\mu\text{s}$  pulse width) and sensing incubation time after the relaxation time  $T = 1\text{ s}$ . **b**, Schematic of waveform corresponding to  $N$ -pulse excitation (identical pulses to part a) with inter-packet pulse separation  $\Delta T$  and sensing the incubation time after the relaxation time  $T = 1\text{ s}$ . **c**, Measured incubation time on a 500-nm-long channel device for single pulse excitation and multiple pulse excitation ( $N = 10$ ) with  $\Delta T = 10\text{ ms}$ ,  $1\text{ ms}$ ,  $100\mu\text{s}$ ,  $10\mu\text{s}$ . The results clearly shows the state manipulation capability with multiple pulse excitation; however, the inter-packet pulse separation plays no role in the state manipulation.



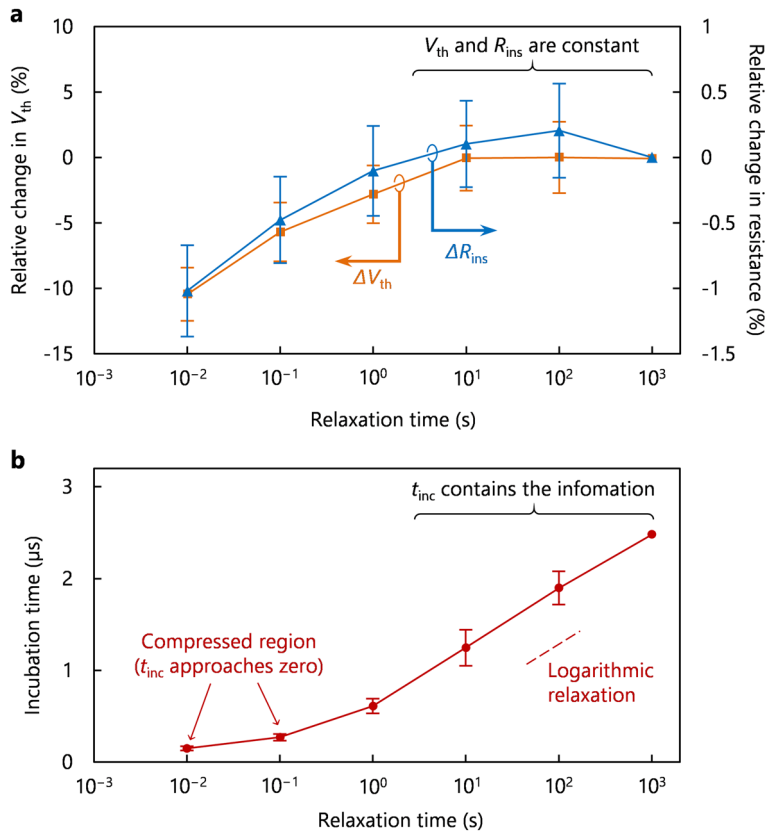
**Extended Data Fig. 5 | Thermal activation of IMT using isolated heaters.** **a**, Optical micrograph of a  $\text{VO}_2$  switch integrated with two electrically isolated heaters. The scale bar corresponds to 10  $\mu\text{m}$ . **b**, Captured thermal micrograph of the device with the heaters triggered at their threshold voltage (18 V). The scale bar corresponds to 10  $\mu\text{m}$ . **c**, Measured temperature over the cutline shown in part B indicating that the temperature at the middle switch (gap) considerably surpasses the IMT temperature. The measurement is done at the steady state; however, considering a sub-microsecond thermal time constant (Extended Data Fig. 1), for a 20- $\mu\text{s}$  long excitation on the heaters, a thermal IMT in the middle switch is expected.



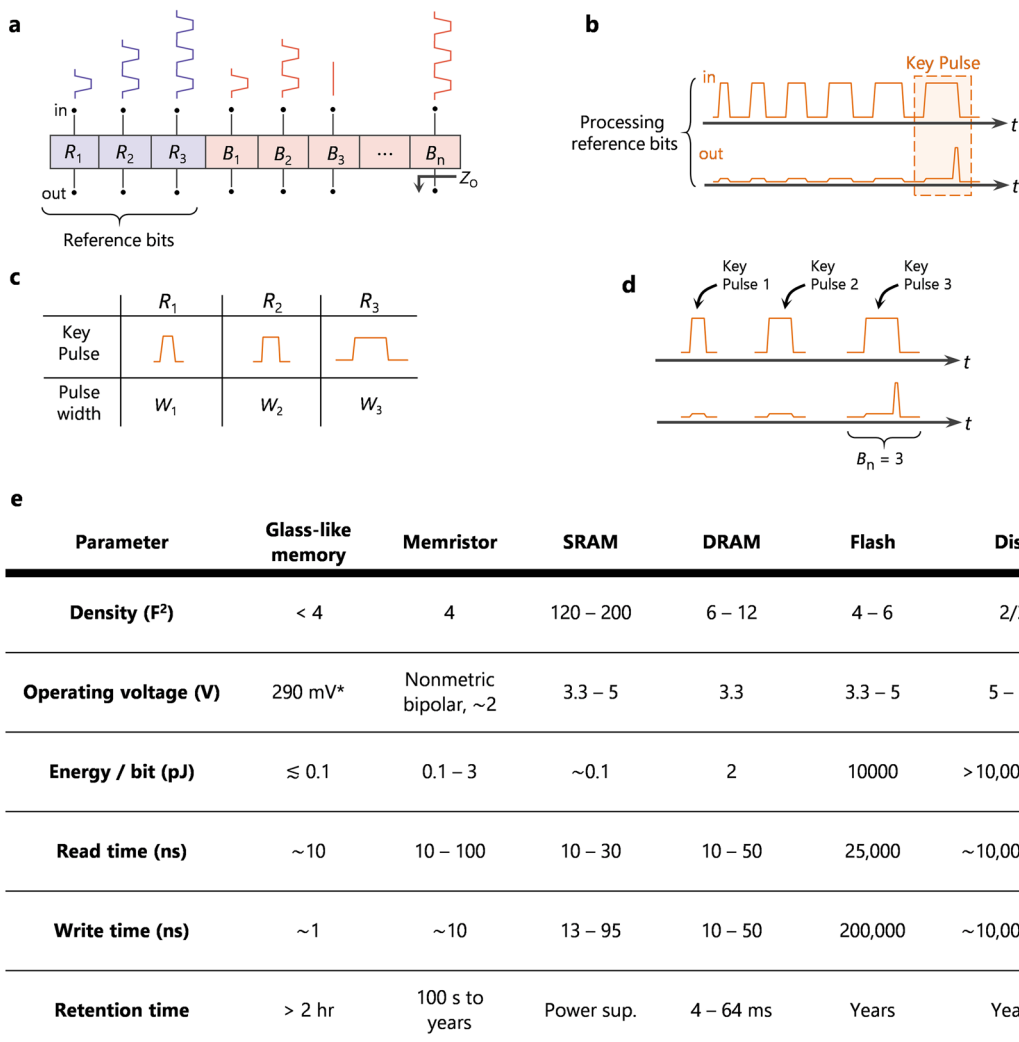
**Extended Data Fig. 6 | In-situ kelvin probe force microscopy to observe possible long-lived metallic domains.** **a**, Illustration of the KPFM experimental setup with in-situ electrical excitation to monitor possible long-lived metallic domains after electrically-driven IMT. If some metallic domains can possibly survive at room temperature and are responsible for the hours-long memory, one expects to capture a nonuniform surface potential map<sup>38</sup>. **b**, Gradient of the KPFM signal corresponding to the post-IMT scanning indicates visually no difference between the VO<sub>2</sub> layer and the metallic pads (serving as reference), which is not supportive for long-lived metallic domains at the resolution of the KPFM scan (~30 nm) to be responsible for the observed memory.



**Extended Data Fig. 7 | Investigation on the effect of VO<sub>2</sub> channel length on the observed memory.** VO<sub>2</sub> switches with different channel lengths ranging from 500 nm down to 50 nm and fixed width of 20  $\mu$ m were investigated. The memory effect was probed by applying double pulses with relaxation times of 10 ms and 1 s. The measured VO<sub>2</sub> current for **a**, 500-nm-long channel VO<sub>2</sub> switch ( $V_{\text{set}} = 2.8$  V). **b**, 200-nm-long channel VO<sub>2</sub> switch ( $V_{\text{set}} = 1.65$  V). **c**, 100-nm-long channel VO<sub>2</sub> switch ( $V_{\text{set}} = 1.25$  V). **d**, 50-nm-long channel VO<sub>2</sub> switch ( $V_{\text{set}} = 0.95$  V). The voltage of each device was set to result in almost identical incubation times in the first reference pulse (blue curves). Despite the considerable difference in the VO<sub>2</sub> channel lengths, the second pulses exhibited similar incubation times. These results show that the memory effect is identical among devices and not a strong function of channel length. This suggests that the observed phenomena are not attributed to any mesoscopic length scale.



**Extended Data Fig. 8 | Evaluation of threshold voltage, resistance and the incubation time of a  $\text{VO}_2$  switch.** **a**, IMT threshold voltage and resistance of a 1- $\mu\text{m}$ -long channel  $\text{VO}_2$  switch measured at different relaxation times. Both parameters show similar trends, although the change in the threshold voltage is ten times larger than that of the resistance. Both parameters stabilize at in a few seconds and do not show logarithmic relaxation. We note that the MIT threshold voltage was totally independent from the relaxation time. **b**, Measured incubation revealed the information of previous switching events when the threshold and resistance are constant. Each data point corresponds to at least 20 measurements (error bars defined) with the exception of the  $T = 1000$  s where we collected three data points. The results show that the memory effect embedded in the incubation time is independent from the changes in the threshold voltage and the resistance of the channel.



\* Record for elevated temperatures. The concept is operational for voltages below 1 V at room temperature.

**Extended Data Fig. 9 | Concept of ultrafast ultra-scaled multilevel glass-like memory in  $\text{VO}_2$ .** **a**, Scheme of a four-level glass-like memory including three reference bits  $R_1$ ,  $R_2$ , and  $R_3$  (written by different number of pulses,  $N_1$ ,  $N_2$ , and  $N_3$ , respectively) and  $n$  ordinary bit  $B_k$ . **b**, Reading process starts by processing the reference bits to extract the pulse width needed to trigger IMT in each reference bit. It is possible to apply a train of pulses with increasing widths until an IMT event takes place: this gives the incubation time corresponding to a  $\text{VO}_2$  switch which is excited by  $N_k$  pulses. It is also possible to apply a longer pulse and measure the IMT time delay (incubation time). A pulse with width equal to the incubation time is able to fire IMT with those bits that are activated with the same number of pulses as the reference bit ( $N_k$ ). We call this a key pulse. **c**, Three key pulses with pulse-widths  $W_1$ ,  $W_2$  and  $W_3$  are obtained ( $W_1 < W_2 < W_3$ ). **d**, Three key pulses are applied to each bit  $B_k$  to accomplish the reading process. **e**, Comparison between the glass-like memory and other technologies.

**Extended Data Table 1 | Verification of the empirical model presented in equation 1 under a non-uniform applied pattern**

Pulse no.	Relaxation time (ms)	Measured $t_{inc}$ (ns)	Reduction in the incubation time with respect to the reference pulse		
			Measurement (ns)	Analytical model (ns)	Error (%)
0 (Reference)	1000	778.4	-	-	-
1	10	639.1	139.3	137.0	1.7%
2	1	571.2	207.2	208.1	0.4%
3	100	680.1	98.3	100.1	1.8%
4	1	572.7	205.7	206.3	0.3%
5	1	559.9	218.5	218.2	0.2%
6	1	552.5	225.9	224.0	0.9%

\*Calculations were presented in the Methods section.